J. Fluid Mech. (1999), *vol.* 391, *pp.* 123–149. Printed in the United Kingdom

Direct simulation of unsteady axisymmetric core–annular flow with high viscosity ratio

By JIE LI AND YURIKO RENARDY

Department of Mathematics and Interdisciplinary Center for Applied Mathematics, Virginia Polytechnic Institute and State University, Blacksburg, VA 24061-0123, USA

(Received 24 September 1998 and in revised form 7 January 1999)

Axisymmetric pipeline transportation of oil and water is simulated numerically as an initial value problem. The simulations succeed in predicting the spatially periodic Stokes-like waves called bamboo waves, which have been documented in experiments of Bai, Chen & Joseph (1992) for up-flow. The numerical scheme is validated against linearized stability theory for perfect core–annular flow, and weakly nonlinear saturation to travelling waves. Far from onset conditions, the fully nonlinear saturation to steady bamboo waves is achieved. As the speed is increased, the bamboo waves shorten, and peaks become more pointed. A new time-dependent bamboo wave is discovered, in which the interfacial waveform is steady, but the accompanying velocity and pressure fields are time-dependent. The appearance of vortices and the locations of the extremal values of pressure are investigated for both up- and down-flows.

1. Introduction

Core–annular flow is a pressure-driven flow through a pipe of one fluid at the core and another fluid in the annulus. This arrangement arises naturally for fluids with markedly different viscosities, because higher viscosity material tends to become encapsulated by lower viscosity material. An industrial application is the lubricated pipelining of crude oil with the addition of water (Joseph & Renardy 1993; Joseph *et al.* 1997). The purpose is to efficiently transport a very viscous liquid, which on its own would require costly work, whereas when the viscous fluid just along the wall is replaced by a much less viscous immiscible one, in this case water, then the work required for transportation is significantly lowered. The ideal arrangement has a perfectly cylindrical interface (figure 1*a*), but a wavy interface is also viable (figure 1*b*). Regimes found experimentally in Bai, Chen & Joseph (1992) include bamboo waves for up-flow, disturbed bamboo waves for both up-flow and down-flow, and corkscrew waves in down-flow.

Our motivation for studying bamboo waves in vertical core–annular flow is that these structures are well-documented in the experiments of Bai *et al.* (1992). Their oil density is 0.905 g cm^{-3}, oil viscosity is 6.01 P, water density is 0.995 g cm^{-3} and water viscosity is 0.01 P. In the bamboo wave regime, trains of sharp crests are connected by long filaments. The waves are axisymmetric and occur in a very robust regime of up-flow, occupying a large area in the up-flow charts shown in figures 16.1–16.4 of Joseph & Renardy (1993). They maintain well-defined average wavelengths and wave speeds. Possible imperfections include the overtaking of one crest by another and the transient stretching of filaments between the waves. The average length of a bamboo wave decreases monotonically as the oil input is increased for fixed

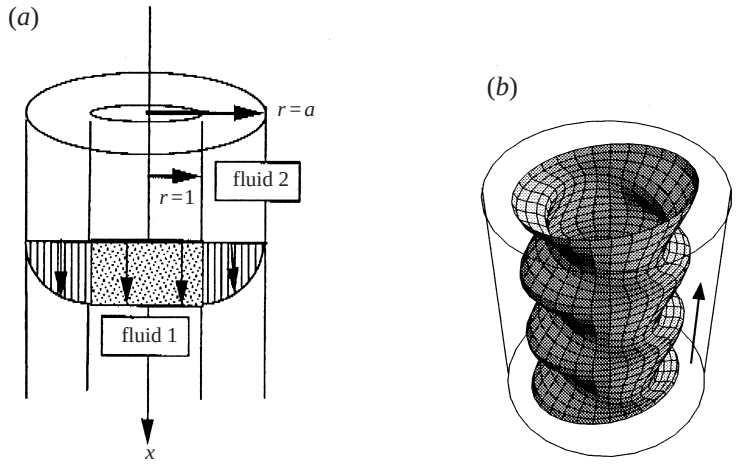

FIGURE 1. (*a*) Schematic of core–annular flow. (*b*) Axisymmetric waves.

flow rate of water. Disturbed bamboo waves are observed when the driving pressure gradient is relatively large and the flow is fast. They are observed in both up-flow and down-flow. The main difference between these flows is that in down-flow, the driving pressure gradient and gravity act in the same direction, making the heavier fluid, water, fall and the buoyancy holds the oil back, while in up-flow, gravity hinders the water and the oil is encouraged to flow upwards. Naturally, if the driving pressure gradient is sufficiently strong and dominant, then the difference between up-flow and down-flow vanishes. Thus the disturbed bamboo waves are observed in both regimes.

The direct numerical simulation of bamboo waves is treated in Bai, Kelkar & Joseph (1996), under the assumptions of steady flow, density matching, and an infinitely viscous core. The core is modelled as a solid which responds to the pressure forces in the water and deforms according to Newton's law. They prescribe the wave speed, the average core radius, and the hold-up ratio. Their iteration begins with an assumed free surface shape, and during each iteration the pressure gradient and wavelength are adjusted. They show their simulations compared with experimental photographs in figures 6–8 of Bai *et al.* (1996). Their simulated waveforms typically have peaks which are more rounded than the experimental form. In addition, the simulated peaks have some asymmetry across them; for example, the steep fronts and gradual tails of figure 7 and the 'flying core flow' of figure 2. The experimental data at the higher speeds, however, show mirror symmetry at the peaks, pointed peaks and flat troughs. This symmetric waveform is reminiscent of solitary waves which were investigated in Renardy (1992) using the KdV equation. In this paper, we simulate the fully coupled liquid–liquid flow, and succeed in predicting the rounded peaks at low speeds and pointed peaks at higher speeds.

In §4, the linearized stability analysis of perfect core–annular flow (Bai *et al.* 1992; Hu & Patankar 1995; Renardy 1997) is revisited in a summary format. The linearized theory reveals the maximum growth rate mode, which has already been correlated with experimental observations in Bai *et al.* (1992) and Joseph & Renardy (1993) for the axisymmetric case. Since the observed wave speeds and wavelengths of the bamboo wave regimes are close to the linear theory, the initial condition for our numerical simulation is seeded with an eigenmode. It is also shown that as the Reynolds number

is increased, the most unstable wavelength shortens. Our full numerical simulations are initialized with an eigenmode, and are tracked through the exponential linear growth rate and into the nonlinear regime. The most unstable eigenmode, as well as less dangerous modes, are tracked.

In §5, the consideration of weakly nonlinear effects close to perfect core–annular flow is summarized (Renardy 1997). When perfect core–annular flow loses stability at a Hopf bifurcation at wavenumber α, an axially travelling wave solution may bifurcate and saturate. The weakly nonlinear terms in the governing equations give rise to the Landau coefficient, via a centre-manifold reduction method, thus determining whether the travelling wave solution is stable/unstable. The Landau coefficient consists of contributions from interactions between the primary mode and its second harmonic, the mean flow mode, and a cubic self-interaction term. This analysis yields the saturation waveform, which allows us to show the weakly nonlinear development of the symmetric waveform at supercritical bifurcations, as precursors of bamboo waves.

In §6, the pressure fields and streamlines are illustrated, and shown to correlate with the cartoon of figure 15.5 of Joseph & Renardy (1993). The location of vortices and pressure maxima/minima are examined in the light of the waveforms. A new time-dependent bamboo wave is discovered. These bamboo waves would appear as steady interface shapes, but the accompanying velocity field is unsteady. This typically arises when the Reynolds number is increased. It is not surprising that a steady solution would then lose stability to time-dependent and eventually chaotic solutions as the flow transitions. However, it is surprising that the time-dependent bamboo waves would appear to the eye to be steady. In §7, we examine bamboo waves in down-flow and show examples of wave shapes which look like the up-flow cases. However, the pressure fields are qualitatively different, and the manner in which the velocity field changes with the Reynolds number is also different from the up-flow case. Although these features of down-flow are interesting in their own right, the path forward in the investigation for down-flow requires the treatment of non-axisymmetric core–annular flow, which is the goal of future work.

2. Numerical scheme

2.1. *Governing equations*

The momentum equations are the axisymmetric Navier–Stokes equations:

$$\rho\left(\frac{\partial u}{\partial t}+u\frac{\partial u}{\partial u}+v\frac{\partial u}{\partial x}\right)=-\frac{\partial P}{\partial r}+\frac{1}{r}\frac{\partial(rS_{rr})}{\partial r}+\frac{\partial S_{xr}}{\partial x}-\frac{S_{\theta\theta}}{r}+F_r, \tag{2.1}$$

$$\rho\left(\frac{\partial v}{\partial t}+u\frac{\partial u}{\partial v}+v\frac{\partial v}{\partial x}\right)=-\frac{\partial P}{\partial x}+\frac{1}{r}\frac{\partial(rS_{rx})}{\partial r}+\frac{\partial S_{xx}}{\partial x}+\rho g+F_x, \tag{2.2}$$

where $S_{rr}=2\mu(\partial u/\partial r)$, $S_{\theta\theta}=2\mu(u/r)$, $S_{xx}=2\mu(\partial v/\partial x)$, $S_{rx}=\mu(\partial v/\partial r+\partial u/\partial x)$, $S_{xr}=S_{rx}=\mu(\partial v/\partial r+\partial u/\partial x)$, The radial and axial components of velocity are denoted $\boldsymbol{u}=(u,v)$, and the pressure by P. The body force $\boldsymbol{F}=(F_r,F_x)$ includes the interfacial tension in the volume-of-fluid (VOF) formulation. Incompressibility yields:

$$\nabla\cdot\boldsymbol{u}=\frac{1}{r}\frac{\partial(ru)}{\partial r}+\frac{\partial v}{\partial x}=0. \tag{2.3}$$

The two fluids are immiscible. Density and viscosity are constant in each phase but may be discontinuous at the interface. We use the VOF scheme. A volume fraction

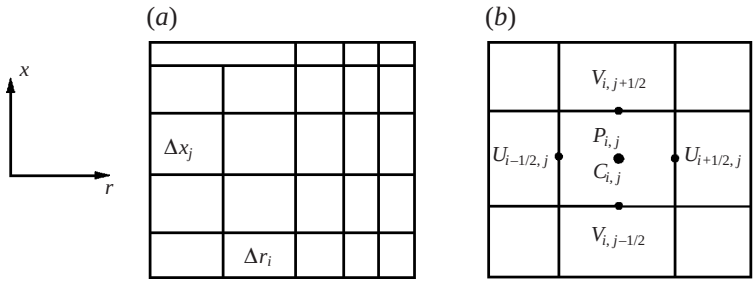

FIGURE 2. (*a*) Two-dimensional Cartesian mesh with variable cell sizes. (*b*) Location of variables in a MAC mesh cell.

field C is used to represent and track the interface, which is transported by the velocity field $\boldsymbol{u}$:

$$\frac{\partial C}{\partial t} + \boldsymbol{u} \cdot \nabla C = 0. \tag{2.4}$$

This equation is used to calculate the density and viscosity. For cells overlying the interface, the average values of density and viscosity are interpolated by the following formulas:

$$\rho = C\rho_1 + (1 - C)\rho_2, \tag{2.5}$$

$$\mu = C\mu_1 + (1 - C)\mu_2. \tag{2.6}$$

2.2. *Discretization*

Our numerical method is based on those of Lafaurie *et al.* (1994), Li (1995), Coward *et al.* (1997), Li, Renardy & Renardy (1998), and Gueyffier *et al.* (1999). Some adjustments are necessary in order to adapt our two-dimensional code to the axisymmetric case. The advection of the interface is treated with a Lagrangian method. Hence, no adjustment is needed here, in contrast to some VOF methods based on the Eulerian formulation, where the formulae for divergence are different for the two-dimensional plane case and the axisymmetric case. Next, we solve the momentum equations by a projection method. In core–annular flow, the pressure P is decomposed into two parts, $P = -fx + p$, where f is the driving pressure gradient. We calculate first an approximate velocity $\boldsymbol{u}^*$ without the pressure gradient ∇p from the momentum equations, assuming that the velocity $\boldsymbol{u}^n$ at time $n\Delta t$ is known:

$$\frac{\boldsymbol{u}^* - \boldsymbol{u}^n}{\Delta t} = -\boldsymbol{u}^n \cdot \nabla \boldsymbol{u}^n + \frac{1}{\rho}(\boldsymbol{f} + \nabla \cdot (\mu \boldsymbol{S}) + \boldsymbol{F} + \rho \boldsymbol{g})^n, \tag{2.7}$$

where the driving pressure gradient $\boldsymbol{f}$ is treated as a body force. In general, the resulting flow field $\boldsymbol{u}^*$ does not satisfy the continuity equation. However, we require that $\nabla \cdot \boldsymbol{u}^{n+1} = 0$ and

$$\frac{\boldsymbol{u}^{n+1} - \boldsymbol{u}^*}{\Delta t} = -\frac{\nabla p}{\rho}. \tag{2.8}$$

Taking the divergence of (2.8), we obtain a Poisson-like equation

$$\nabla \cdot \left(\frac{\nabla p}{\rho}\right) = \frac{\nabla \cdot \boldsymbol{u}^*}{\Delta t} \tag{2.9}$$

which is used to find the pressure field. Next, $\boldsymbol{u}^*$ is corrected using this pressure field and the updated solution $\boldsymbol{u}^{n+1}$ is found from (2.8).

We use an Eulerian mesh of rectangular cells having variables sizes, Δx_i for the ith x-direction mesh size, Δy_j for the jth y-direction mesh size, as illustrated in figure 2. The spatial discretization of the variables u, v and p is based on the MAC method. The non-conservative scheme is chosen for the advective terms. The pressure and viscous terms in the momentum equations are calculated using second-order central finite differences, taking into account the variable mesh. In a MAC mesh, the variables are not defined at the same location. This apparently sophisticated mesh presents the advantage that in the resulting discrete Poisson equation, the pressure field is not decoupled and its solution permits no checkerboard oscillation. Furthermore, no numerical boundary condition is needed for the pressure if the one for the velocity is given. As pointed out in Li *et al.* (1998), the solution of the discrete counterpart of Poisson's equation (2.9) is the most time-consuming part of our Navier–Stokes solver and, consequently, an efficient solution is crucial for the performance of the whole method. The multigrid method is arguably the most efficient: to reduce the error in the discretization of Poisson's equation by a constant, the multigrid method requires a fixed number of iterations, independent of the mesh size. Our multigrid Poisson solver for the two-dimensional case carries over to the axisymmetric case, the only exception being that two coefficients in the radial direction of Poisson's equation need to be adjusted, because the formula for the divergence differs from the two-dimensional plane case. The discretization of the incompressibility condition (2.3) at cell (i, j) is

$$\frac{1}{r_i}\frac{r_{i+1/2}u_{i+1/2} - r_{i-1/2}u_{i-1/2}}{\Delta r_i} + \frac{v_{i,j+1/2} - v_{i,j-1/2}}{\Delta x_j} = 0, \tag{2.10}$$

where $r_{i-1/2}$ denotes the left face coordinate of cell (i, j), $r_{i+1/2}$ the right face coordinate and $r_i = \frac{1}{2}(r_{i-1/2} + r_{i+1/2})$. Finally, the CSF technique (Brackbill, Kothe & Zemach 1992) for the treatment of interfacial tension has been adapted for the axisymmetric case here.

2.3. *Stability and semi-implicit Stokes solver*

Two necessary conditions for stability of the above explicit projection method on the MAC mesh (Peyret & Taylor 1990) are:

$$\Delta t \leqslant \frac{Re}{2}\frac{\Delta x^2 \Delta y^2}{\Delta x^2 + \Delta y^2}, \quad \Delta t \leqslant \frac{4}{Re}\frac{1}{(|u| + |v|)^2},$$

where Re is the Reynolds number. The first inequality expresses the restriction placed by viscous terms upon the time step size, while the second expresses the restriction by convection terms. In this paper, we treat core–annular flow, using the physical parameters for the experimental oil and water (Bai *et al.* 1992) as described in the Introduction. The viscosity of oil is very different from that of water, while the densities are similar. The Reynolds number for the water annulus is roughly 600 times that of the core oil; the large Reynolds number in the water and the much smaller Reynolds number in the oil impose severe restrictions on the time step size, according to the stability criteria for the explicit formulation. This suggests the implementation of the following implicit scheme for the viscous terms.

We have developed an efficient and unconditionally stable method for the viscous terms in two-dimensional plane flow (Li *et al.* 1998), which is adapted in the following

way to the axisymmetric case:

$$\rho\frac{u^{n+1}-u^n}{\Delta t}=\frac{1}{r}\frac{\partial}{\partial r}\left(2\mu\frac{\partial u^{n+1}}{\partial r}\right)+\frac{\partial}{\partial x}\left(\mu\left(\frac{\partial v^n}{\partial r}+\frac{\partial u^{n+1}}{\partial x}\right)\right)-2\mu\frac{u^{n+1}}{r^2}+\ldots, \quad (2.11)$$

$$\rho\frac{v^{n+1}-v^n}{\Delta t}=\frac{1}{r}\frac{\partial}{\partial r}\left(r\mu\left(\frac{\partial v^{n+1}}{\partial r}\right)\right)+\frac{\partial}{\partial r}\left(\mu\left(\frac{\partial u^n}{\partial x}\right)\right)+\frac{\mu}{r}\frac{\partial u^{n+1}}{\partial x}+\frac{\partial}{\partial x}\left(2\mu\left(\frac{\partial v^{n+1}}{\partial x}\right)\right)+\ldots, \quad (2.12)$$

where the terms indicated by dots are the inertial terms which are treated explicitly. In contrast to the two-dimensional scheme, $\partial u^{n+1}/\partial x$ is included in the implicit part of (2.12). The scheme will not be unconditionally stable if it is in the explicit part, because there is no term to compensate for it. Thus v is coupled to u implicitly, but u depends on v only explicitly. The term $\partial u^{n+1}/\partial x$ in the implicit part of (2.12) does not reduce the efficiency of our method. From equation (2.11), we first solve for u^{n+1}, which is decoupled from v^{n+1}. Next, we substitute for u^{n+1} in the right-hand side of equation (2.12) and solve for v^{n+1}. The factorization technique discussed in Li *et al.* (1998) applies also to our scheme (the error of factorization is of order $O(\Delta t^3)$), so we need only to solve a tridiagonal system and this results in a significant reduction in computing and memory.

As far as the viscous terms are concerned, our semi-implicit scheme is unconditionally stable. To see this, let $u \sim \exp(\mathrm{i}\alpha r + \mathrm{i}\beta x)$ and let $\mu = 1, \rho = 1$ for simplicity. Equations (2.11)–(2.12) yield the following matrix equation from the viscous terms, ignoring lower-order terms:

$$\begin{pmatrix} 1+\Delta t(2\alpha^2+\beta^2+2/r^2-2\alpha\mathrm{i}/r) & 0 \\ -\Delta t(\beta\mathrm{i}/r) & 1+\Delta t(\alpha^2+2\beta^2-\alpha\mathrm{i}/r)\end{pmatrix}\begin{pmatrix}u^{n+1}\\ v^{n+1}\end{pmatrix} = \begin{pmatrix}1 & -\Delta t\alpha\beta\\ -\Delta t\alpha\beta & 1\end{pmatrix}\begin{pmatrix}u^n\\ v^n\end{pmatrix}. \quad (2.13)$$

The stability analysis is carried out as follows. In equation (2.13), the left-hand-side matrix is essentially diagonal, because the off-diagonal term can be handled as a perturbation, so that the equation has the form $\boldsymbol{A}\boldsymbol{u}^{n+1} = \boldsymbol{B}\boldsymbol{u}^n$. Denote the eigenvalues of $\boldsymbol{A}$ by λ_1^A and λ_2^A, and those of $\boldsymbol{B}$ by λ_1^B and λ_2^B; then

$$|\boldsymbol{A}\boldsymbol{u}^{n+1}| \geqslant \min(|\lambda_1^A|, |\lambda_2^A|)|\boldsymbol{u}^{n+1}|, \quad \text{and} \quad |\boldsymbol{B}\boldsymbol{u}^n| \leqslant \max(|\lambda_1^B|, |\lambda_2^B|)|\boldsymbol{u}^n|.$$

Therefore

$$|\boldsymbol{u}^{n+1}| \leqslant \frac{\max(|\lambda_1^B|, |\lambda_2^B|)}{\min(|\lambda_1^A|, |\lambda_2^A|)}|\boldsymbol{u}^n| < |\boldsymbol{u}^n|.$$

Specifically, the eigenvalues of the left-hand matrix in equation (2.13) are $1+\Delta t(2\alpha^2+\beta^2+2/r^2-2\alpha\mathrm{i}/r)$ and $1+\Delta t(\alpha^2+2\beta^2-\alpha\mathrm{i}/r)$, while the eigenvalues of the right-hand matrix are $1+\Delta t\alpha\beta$ and $1-\Delta t\alpha\beta$. From an elementary calculation, we can show that the magnitude of both eigenvalues of $\boldsymbol{A}$ are larger than the magnitude of the two eigenvalues of $\boldsymbol{B}$. This stability is absolutely indispensable for our numerical study of high-viscosity-ratio flows.

3. Core–annular flow equations and parameters

Consider the perfect core–annular flow (PCAF) of figure 1. In dimensional terms, the pipe radius is denoted R_2, the base velocity field is $(0, V_i^*(r^*))$, where asterisks denote dimensional variables and $i = 1, 2$. The undisturbed interface position is

$r = R_1$, where $P_2^* - P_1^* = T^*/R_1$, T^* is the interfacial tension. The pressure gradient in the axial direction is a constant: $\mathrm{d}P^*/\mathrm{d}x = -f^*$. The following are four dimensionless parameters:

$$m = \mu_2/\mu_1, \quad a = R_2/R_1, \quad \zeta = \rho_2/\rho_1, \quad K = (f^* + \rho_1 g)/(f^* + \rho_2 g), \tag{3.1}$$

where K measures the ratio of driving forces in the core and annulus. Dimensionless variables are chosen to be $(r, x) = (r^*, x^*)/R_1$, $(u, v) = (u^*, v^*)/V_0^*(0)$, $t = t^* V_0^*(0)/R_1$, $P = P^*/[\rho_1 V_0^{*2}(0)]$, where the centreline velocity is

$$V_0^*(0) = (f^* + \rho_2 g)\frac{R_1^2}{4\mu_2}A, \quad A = mK + a^2 - 1 + 2(K-1)\log a. \tag{3.2}$$

The dimensionless base velocity field is $(0, V(r))$ where

$$V(r) = \begin{cases} [a^2 - r^2 - 2(K-1)\log(r/a)]/A, & 1 \leqslant r \leqslant a \quad \text{(annulus)} \\ 1 - mr^2 K/A, & r < 1 \qquad\quad \text{(core)}. \end{cases} \tag{3.3}$$

An interfacial tension parameter is $J = T^* R_1 \rho_1/\mu_1^2$. Reynolds numbers Re_i are defined by $Re_i = \rho_i V_0^*(0) R_1/\mu_i$, $i = 1, 2$, where $Re_1/Re_2 = m/\zeta$. In summary, PCAF is characterized by six dimensionless parameters: m, a, ζ, J, K and Re_1.

Perfect core–annular flow can lose stability to a variety of regimes. Several qualitatively different regimes of flow have been documented in the experiments of Bai *et al.* (1992), which were conducted at 22°C, with pipe diameter $\frac{3}{8}$ in., $m = 1/601$, $\zeta = \rho_\mathrm{w}/\rho_\mathrm{o} = 0.995/0.905 = 1.10$, $R_2 = \frac{3}{16}$ in. $= 0.47625$ cm, $T^* = 8.54$ dyn cm^{-1}, $J^* = \rho_\mathrm{o} T^* R_2/\mu_\mathrm{o}^2 = 0.102$, $F = f/(\rho_1 g)$, where subscript w denotes water and o oil. The parameters of Bai *et al.* (1992) are related to ours via

$$J = \frac{\rho_\mathrm{o} T^* R_1}{\mu_\mathrm{o}^2} = \frac{J^*}{a}, \quad K = \frac{f + \rho_1 g}{f + \rho_2 g} = \frac{1 + F}{\zeta + F}.$$

The experiments were conducted in a vertical inverted loop. The oil in vertical flow is lighter than water so that buoyancy and the pressure gradient act in the same sense in up-flow, where the core oil is observed to produce bamboo waves, and in the opposite sense in down-flow, where the core is compressed and buckles into corkscrew waves (Renardy 1997). The flow type is determined by two independent parameters. In experiments, Bai *et al.* (1992) prescribe the volume flow rates of water and oil, denoted by Q_w and Q_o, respectively. This is equivalent to prescribing the two superficial velocities V_w and V_o. The superficial water velocity is defined by $V_\mathrm{w} = Q_\mathrm{w}/A$, and the superficial oil velocity by $V_\mathrm{o} = Q_\mathrm{o}/A$. Here, $A = \pi R_2^2$ is the cross-sectional area of the pipe. The flow chart of Bai *et al.* (1992) for up-flow is reproduced in figure 3 for convenience.

The hold-up ratio h, defined as the ratio of the input oil–water ratio to the *in situ* oil–water ratio, is an important practical parameter for core–annular flow. Experiments show that h is constant in up-flow and fast flows. The radius ratio a is related to the flow rates via the hold-up ratio h. If the flow is perfectly core–annular, then the dimensionless cross-sectional areas are πa^2 and π, respectively, which yields the *in situ* water-to-oil ratio, $a^2 - 1 = hQ_\mathrm{w}/Q_\mathrm{o}$ simply by definition of h. Therefore,

$$a = \sqrt{1 + hQ_\mathrm{w}/Q_\mathrm{o}} = \sqrt{1 + hV_\mathrm{w}/V_\mathrm{o}}. \tag{3.4}$$

In order to set up the parameters and compare to experiments, Bai *et al.* (1992) determine the perfect core–annular flow which would correspond to the prescribed values of two experimental parameters: V_w and V_o, or a and V_o. Perfect core–annular

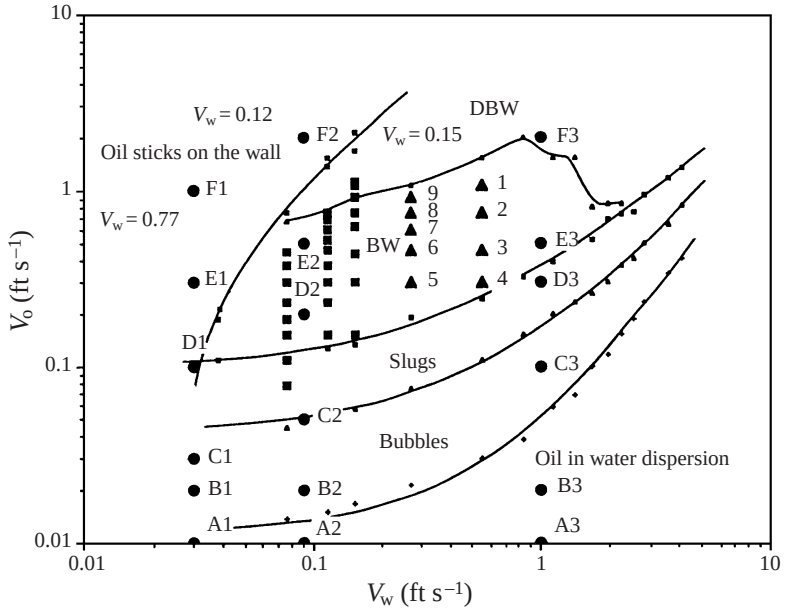

FIGURE 3. This flow chart (from Bai *et al.* 1992) shows the types of flow that arise in up-flow as function of the superficial oil velocity V_o and the superficial water velocity V_w.

flow is determined by two independent quantities in both experiments and theory. Two alternative methods were used in Bai *et al.* (1992) to make the comparison: by fixing values of V_o and V_w, or by fixing values of V_o and a. There may be a sizable difference between these two approaches for the same experiment. As an example, take flow regime no. 1 of figure 3, where $V_o = 1.06$ ft s^{-1} and $V_w = 0.55$ ft s^{-1}: the value of a calculated from equations (18.15) and (18.16) of Joseph & Renardy (1993) is 1.61, but the experimental value of a (from formula (3.4) with hold-up ratio $h = 1.39$) is 1.31. Although they claim to have consistent results from the two methods, in our opinion, their comparisons by fixing V_o and a provide better agreement with experiments with regard to wave speed. The physical parameters that define PCAF will change with the flow in the nonlinear regime, so that there is no reason that a PCAF with parameters V_o and V_w would evolve to nonlinear waves keeping the same values of V_o and V_w. However, since the flow is incompressible, the quantities of oil and water must be conserved. It is hence judicious to prescribe the parameter a instead of V_w. Conservation of volume also implies that the parameter a will remain constant as the PCAF evolves into the nonlinear regime. The evolution is, however, more complicated for superficial velocities V_o and V_w. In the cases we study here, water is heavier than the oil and moves slowly in comparison with the oil in the upward direction. As the PCAF evolves into the nonlinear regime, the interface shape waves and the friction between oil and water increases. As a consequence, the oil core could be slowed down significantly by water. The evolution into the nonlinear regime has two opposing effects on the water motion. On the one hand, the wavy interface traps water in its troughs and carries the water with it, which tends to increase the water volume flow rate. On the other hand, the oil drag force is one of the important factors contributing to the water volume flow rate. As the oil core is slowed down in the nonlinear

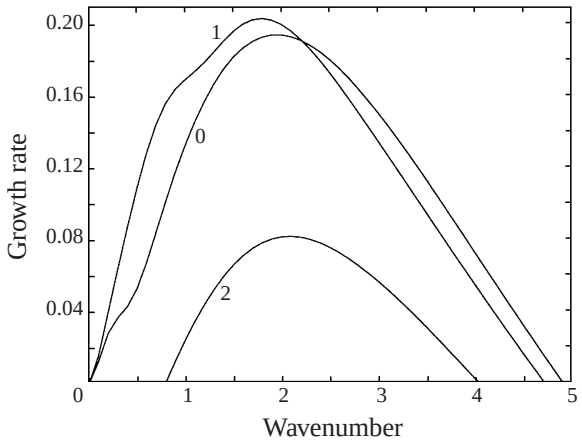

FIGURE 4. $Re_1 = 0.93$, $a = 1.28$, $m = 0.00166$, $\zeta = 1.1$, $J = 0.0795$, $K = -0.4552$. Theoretical linear growth rates vs wavenumber for azimuthal modes 0,1,2. Higher modes are stable.

regime, this force decreases, which tends to reduce the water volume flow rate. With these mechanisms acting on the flow rate, it is not obvious what the correspondence is, between the PCAF V_o and the V_o in the resulting nonlinear flow. Thus, simply prescribing the experimental quantities V_o and V_w to initialize PCAF is naive.

4. Numerical study of small perturbations

In this Section, we study the linear growth regime of perfect core–annular flow. The base solution is perturbed so that the total solution is $(u, V + v)$, $P + p$, the interface position is $1 + \delta(x, t)$, and perturbations are proportional to $\exp(i\alpha x + \sigma t)$ (Renardy 1997). Experimental results for wave speeds and wavelengths have been compared with linear theory (Bai *et al.* 1992; Joseph & Renardy 1993), even though the regimes are obviously highly nonlinear. We begin our numerical study with the experimental figure 6 of Bai *et al.* (1996). The two quantities prescribed in this flow are $[Q_w, Q_o] = [200, 429]$ cm^3 min^{-1}. The parameters for the corresponding PCAF are first calculated using the fixed values of V_o and a. The experimental hold-up ratio h is 1.39 for this flow, and from equation (3.4), we obtain the corresponding value of $a = 1.28$. The superficial oil velocity is $V_o = 10$ cm s^{-1}. We can then calculate the other parameters of PCAF flow via equation (18.15) of Joseph & Renardy (1993) and other appropriate formulas. We obtained the parameters $Re_1 = 0.93$, $m = 0.00166$, $\zeta = 1.1$, $J = 0.0795$ and $K = -0.4552$. The theoretical growth rates for azimuthal mode 0, 1 and 2 versus wavenumber are shown in figure 4. Higher modes are stabilized by interfacial tension. The non-axisymmetric mode 1 attains the highest growth rate, and hence a non-axisymmetric wave is expected to occur. However, mode 1 is only a little more unstable than the axisymmetric mode. For a well-controlled experiment in which the axisymmetric mode is favoured, bamboo waves may be observed. From figure 4 we see that the growth rate of mode 0 reaches its maximum at wavenumber $\alpha = 2.0$. This is the most dangerous axisymmetric mode. Linear theory indicates that the growth rate is $Re(\sigma) = 0.1940$ and the wave speed is $c = 0.851$ for this wavenumber.

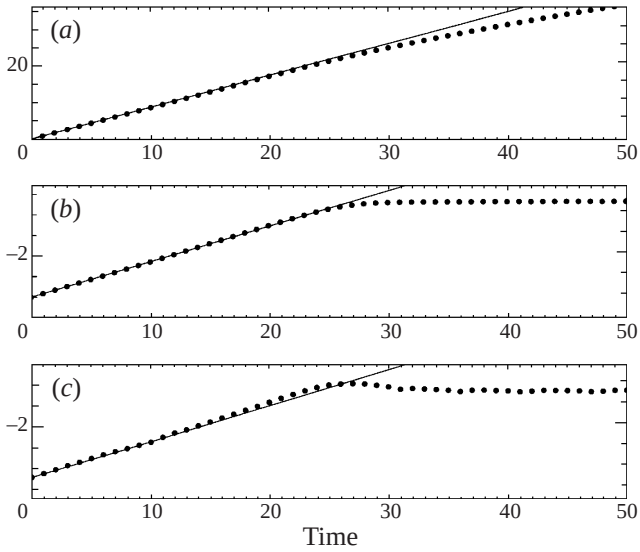

FIGURE 5. Plot of crest position (a) and log plots of the maximum of interface position (b), and the maximum of the radial velocity U (c) against time for the flow $Re_1 = 0.93$, $a = 1.28$, $m = 0.00166$, $\zeta = 1.1$, $J = 0.0795$, $K = -0.4552$ and $\alpha = 2.0$. Theoretical linear growth rate for the interfacial mode is 0.1940. Solid lines represents theoretical growth and circles represent the calculation. The calculation is carried out on a 256×256 mesh.

The growth rate predicted by linear theory for mode 0 with wavenumber 2.0 is compared with the numerical simulation. We initialize our simulation with a very small perturbation amplitude $A(0) = 0.001$, in order to keep the flow in the linear regime for a relatively long time. Figure 5(a) shows the crest position vs. time. The linear regime persists until roughly $t = 25$ where the numerical wave speed is 0.8369, with 1.6% difference compared to the theoretical value. Figure 5(b) shows, on a $\log_{10}$-linear scale, the evolution of the maximum amplitude $A(t)$ with time. Until $t = 25$, the numerical and theoretical growth rates agree, the difference between them being 1%, and the agreement zone is about two decades.The evolution of the maximum of the radial velocity U with time is shown also in figure 5(c) and good agreement is also obtained, the difference between them being 3%. This calculation is carried out on a 256×256 mesh. Recall that for two-layer Couette flow of fluids with moderate viscosities at low speeds (Li *et al.* 1998), small perturbations tended to develop into nonlinear fingers rather than to evolve according to linear theory. To our surprise, we find that the growth rate from linear theory predicts very well the actual evolution of small perturbations in this high-viscosity-ratio flow.

5. Weakly nonlinear bifurcation analysis

When weakly nonlinear effects are taken into account, the bifurcation from perfect core–annular flow to one with axially travelling waves is described in the Appendices in Renardy (1997). This contains the derivation of the Landau equation and definition of the operators. The governing equations, interface and boundary conditions are represented schematically in the form $\mathrm{L}\Phi = \mathrm{N}_2(\Phi, \Phi) + \mathrm{N}_3(\Phi, \Phi, \Phi)$, where $\mathrm{L}, \mathrm{N}_2, \mathrm{N}_3$ are the linear, quadratic and cubic operators, respectively, and Φ is the perturbation to the base flow. The perturbation solution Φ can be decomposed in the

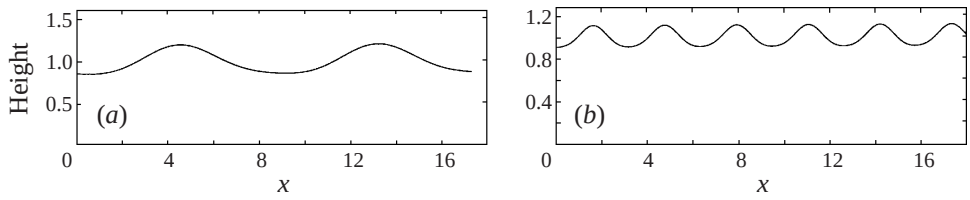

FIGURE 6. Up-flow, $m = 0.00166$, $\zeta = 1.1$: (*a*) $a = 1.61$, $\alpha = 0.725$, $Re_1 = 1$, $K = -2.030303$, $J = 0.0633554$, saturation amplitude 1.20; (*b*) $a = 1.28$, $\alpha = 2$, $Re_1 = 0.93$, $K = -0.4552$, $J = 0.0795$, saturation amplitude 1.11.

form $\Phi = z_1\zeta_1 + \bar{z}_1\bar{\zeta}_1 + 2\mathrm{Re}\ (z_1 z_1\psi_{11} + z_1\bar{z}_1\chi_{11}) + \cdots$, where z_1 is the complex time-dependent amplitude function, ζ_1 is the axisymmetric onset mode of wavenumber α and eigenvalue σ, χ_{11} represents the secondary mean flow mode, ψ_{11} represents the second harmonic, and the dots indicate terms of higher than quadratic order. The dynamics projected onto the centre manifold yield $\mathrm{d}z_1/\mathrm{d}t = (\mathrm{i}\omega + \epsilon_1)z_1 + \beta_1(\lambda)|z_1|^2 z_1$, where the Landau coefficient is $\beta_1(\lambda) = (b_1, 2\mathrm{N}_2(\bar{\zeta}_1, \psi_{11}) + 4\mathrm{N}_2(\zeta_1, \chi_{11}) + 3\mathrm{N}_3(\zeta_1, \zeta_1, \bar{\zeta}_1))$, the bifurcation parameter ϵ_1 is real, and b_1 is the eigenfunction to the adjoint problem (Renardy 1997). In the weakly nonlinear theory, the primary mode interacts with itself and its complex conjugate through the quadratic and cubic nonlinearities in the governing equations, thus generating a secondary mean flow mode χ_{11} and a second harmonic ψ_{11}. These in turn interact with the primary mode through the quadratic terms, and are balanced with the terms generated by the primary mode interacting with itself in the cubic terms of the equations. The first term in β_1 arises from an interaction of the primary mode with the second harmonic, the second term is an interaction of the primary mode with the secondary mean flow, and the third term represents a cubic self-interaction. To reconstruct the nonlinear waveform, we refer to the interface perturbation component h in the eigenfunction ζ_1 and the second harmonic ψ_{11}. We may picture the total interface perturbation as

$$\Phi_h = 2\mathrm{Re}[z_1(t)h(\zeta_1)\exp(\mathrm{i}\alpha x + \mathrm{iIm}\sigma t) + z_1^2(t)h(\psi_{11})\exp(2\mathrm{i}\alpha x + 2\mathrm{iIm}\sigma t)], \tag{5.1}$$

where ψ_{11} contributes $\sin 2\alpha x$ to the interface shape. The travelling wave solution is predicted to saturate when the real part of the Landau coefficient β_1 is negative. When the travelling wave solution is denoted $z_1(t) = \exp(\mathrm{i}\omega t)Z_0$, it saturates at

$$|Z_0| = \sqrt{-\mathrm{Re}\sigma/\mathrm{Re}\beta_1}. \tag{5.2}$$

The total saturation amplitude for the weakly nonlinear waveform is the maximum of Φ_h.

The cases we illustrate in §6 for up-flow are for viscosity ratio $m = 0.00166$, density ratio $\zeta = 1.1$. The linearized stability theory of the previous Section is used to determine the maximum growth rate mode. At that mode, the calculation for the saturation waveform is performed. The bifurcations are supercritical and the bifurcated travelling wave solutions are shown in Figure 6. As the Reynolds number increases past onset and growth rates increase, we eventually expect the weakly nonlinear theory to deviate from the simulations. Figure 6(*a*) corresponds to the experimental situation of data point 1 on the flow chart figure 3 and discussed further in §6. Figure 6(*b*) corresponds to the experimental situation of figure 6 of Bai *et al.* (1996) discussed in §4. Both waveforms show the incipient bamboo wave structure with symmetry across the peaks.

α	0.5	1.0	1.5	1.75	2.0	2.5	3.0	4.0
Re(σ)	0.05324	0.1324	0.1815	0.1917	0.1940	0.1803	0.1505	0.0717
Speed c	0.3944	0.6655	0.7822	0.8205	0.8509	0.8952	0.9243	0.9694
Amplitude		0.2077	0.2005	0.1922	0.1776			

TABLE 1. $Re_1 = 0.93$, $a = 1.28$, $m = 0.00166$, $\zeta = 1.1$, $J = 0.0795$, $K = -0.4552$, axisymmetric mode. At each wavenumber, the theoretical linear growth rate and wave speed are given. The final amplitudes of nonlinear bamboo waves are given for wavenumbers 1 to 2, relevant to experimental length scales.

6. Direct simulation of the experimental regime

For a direct comparison with experiments, one should investigate the spatial evolution of the core–annular flow. This approach has the advantage that we can prescribe the experimental quantities V_o and V_w as entrance conditions. Unfortunately, this kind of simulation is not yet possible due to the computational cost, because the pipeline in Bai *et al.* (1996) is too long in comparison with its cross-sectional radius. We therefore choose a simpler approach, by investigating the temporal evolution of this flow. We suppose that the flow is spatially periodic and we determine the wavelength of the waves by examining the experiment data. We begin with the case studied in §4, for comparison with the experimental figure 6 of Bai *et al.* (1996), with $[a, V_o] = [1.28, 10.00 \text{ cm s}^{-1}]$. The experimental snap-shot shows the coexistence of waves with different wavenumbers, from roughly 1.5 to 2.0. In table 1, theoretical growth rates and wave speeds, and amplitudes of the final bamboo waves are listed against the wavenumber. Numerical simulations are performed by initializing with wavenumbers 1.0, 1.5, 1.75 and 2.0, which is the range relevant to the experimental situation. Very good agreement with the linear theory has been obtained in each case. Beyond the linear regime, these core–annular flows evolve into bamboo waves with constant amplitudes. Their final amplitudes are listed in the bottom row of table 1. The final amplitude decreases with the wavenumbers. Our results show that bamboo waves arise for a range of wavenumbers, not necessarily the one of largest growth rate; this explains in part the coexistence of waves with very different wavelengths. These waves move with different wave speeds and the overtaking of one crest by another is frequently observed in experiments.

Figure 7 illustrates our wave shapes for these four wavenumbers in the nonlinear regime. One of the prominent features is that although the solutions shown here are not steady solutions, the interface shapes are nearly steady, and would appear to be steady to an observer. There is an adjustment period, while the interface shape changes from the initial cosine shape to the bamboo shape. Thereafter, changes in the wave shape are not discernible to the unaided eye, while the accompanying velocity and pressure fields continue to evolve. The steady solution calculated by Bai *et al.* (1996) under solid-core and density-matching assumptions produces an interface shape like the one found in their experiment. However, their interface shape is too rounded and smooth compared to their experimental snap-shot, which shows an almost symmetric form of the crest, with a pointed peak. The crest is slightly sharper on the front and less sharp on its back. These details are successfully reproduced in our results.

The corresponding PCAF base velocity profile is shown in figure 8(*a*). This is a

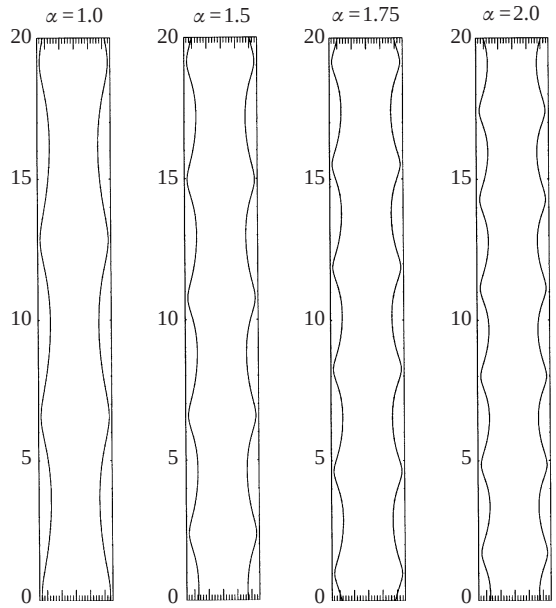

FIGURE 7. Bamboo wave flow for $Re = 0.93$, $a = 1.28$, $m = 0.00166$, $\zeta = 1.1$, $J = 0.0795$ and $K = -0.4552$. The accompanying velocity and pressure fields are time-varying. The interface shapes are almost equilibrated and appear steady.

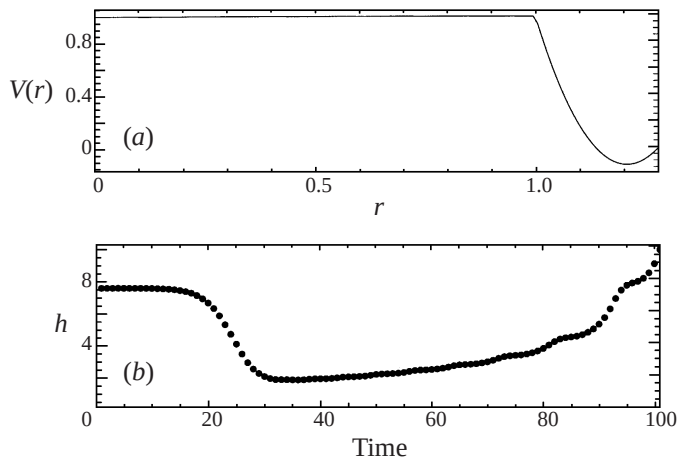

FIGURE 8. (*a*) The velocity profile of PCAF for $Re = 0.93$, $a = 1.28$, $m = 0.00166$, $\zeta = 1.1$, $J = 0.0795$ and $K = -0.4552$. (*b*) The calculated hold-up ratio h against time. Initially, the PCAF hold-up ratio $h = 7.60$. As PCAF evolves into the nonlinear bamboo regime, h decreases first and reaches the minimum value 1.80 at $t = 30$. Thereafter, it increases, reaching 10 at $t = 100$. The experimental value is 1.39.

mixed flow, up for oil and water near the oil core, down for water near the pipe wall. The positive flow rate in the up-flowing portion of water is cancelled in part by the negative flow rate in the down-flowing water, and therefore the resulting water flow rate is small. As a consequence, the PCAF hold-up ratio is 7.60, much greater than the experimental value 1.39. The evolution of the hold-up ratio is shown in figure 8(*b*) for perturbation wavenumber 2. The shape of the interface remains steady

for time roughly larger than 40, after the initial adjustment from the linear regime, and the bamboo wave in figure 7 describes the shape thereafter. The velocity field, on the other hand, continues to evolve. The hold-up ratio decreases very slowly in the linear regime (before time $t = 20$). The dramatic decrease of the hold-up ratio occurs between $t = 20$ and $t = 30$, which corresponds to the transition of core–annular flow from the linear regime to the nonlinear regime. It reaches the minimum value 1.80 at time $t = 30$. During this period, the oil core is slowed down and accordingly the oil flow rate Q_o decreases; on the other hand, the water flow rate Q_w increases because the interface undulation is amplified and more and more water is trapped in the wave troughs. The dramatic reduction of hold-up ratio occurs between $t = 20$ and $t = 30$. Figures 5(*b*) and (*c*) show that this period corresponds to the transition period from the linear regime to the nonlinear regime. The oil core is slowed down significantly at this time. As the oil begins to drag less water, the down-flow of water becomes more significant and plays a dominant role in determining the water flow rate. After $t = 30$, the oil flow rate continues to decrease, but the water flow rate decreases much faster. Therefore, the hold-up ratio rises again. At $t = 100$, it reaches 10, far away from the experimental value 1.39.

By prescribing V_o to initialize PCAF, our simulation fails to predict the experimentally measured value of the hold-up ratio. The principle reason is that the driving pressure force is not big enough to support the up-flow of water. Consideration of a limiting case can shed some light on this phenomenon. Suppose that the two fluids are well mixed and let ρ_c be the average density:

$$\rho_c = \frac{1}{a^2}(\rho_1 + (a^2 - 1)\rho_2),$$

so that the force acting on the mixed fluid is

$$f + \rho_c g = \frac{1}{a^2}((f + \rho_1 g) + (a^2 - 1)(f + \rho_2 g)) = \frac{f + \rho_2 g}{a^2}(K + a^2 - 1).$$

This force must be positive for up-flow. The critical value of K is $K_c = 1 - a^2$. Applying parameters $a = 1.28$ and $K = -0.4552$ to the above, we have

$$f + \rho_c g = \frac{f + \rho_2 g}{a^2}(-0.4552 + 1.28^2 - 1) = 0.1832\frac{f + \rho_2 g}{a^2}.$$

$f + \rho_c g$ is therefore negative when $f + \rho_2 g < 0$. Although in a core–annular up-flow, the driving pressure gradient does not need to be so strong, the critical value $K_c = 1 - a^2$ provides a rule of thumb. The driving pressure is evidently not strong enough at Reynolds number 0.93. The oil core in the nonlinear regime is slowed down and can not provide the force to drag the water up as it does in PCAF, and hence the water falls throughout the annulus. We come to the same conclusion as Bai *et al.* (1992) when they compared PCAF to their experiments: bamboo waves require a much greater pressure gradient to transport a given volume flux of oil than the ideal case PCAF.

Since V_o and V_w are not constant quantities as PCAF evolves into the nonlinear regime, prescribing the experimental values V_o and V_w recorded in the nonlinear regime to PCAF has potentially the consequence of underestimating the pressure gradient of the corresponding PCAF, and hence the Reynolds number. In order to compare with experiment, it will be wise to prescribe two quantities independent of the state of flow. The parameter a is a good candidate. We can choose another parameter such as the experimentally measured pressure gradient f. This quantity can

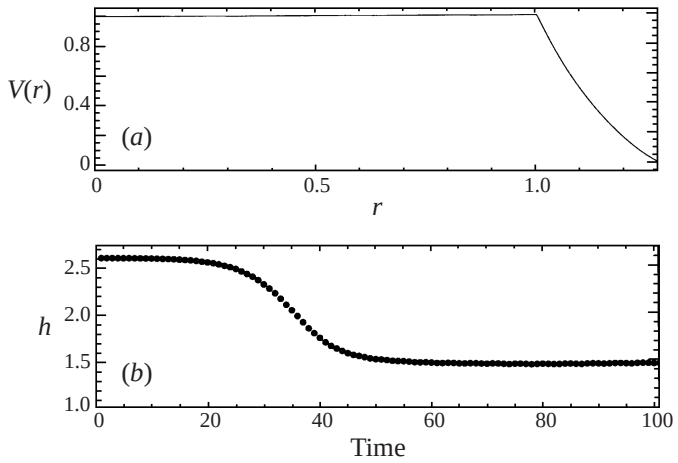

FIGURE 9. (*a*) The velocity profile of PCAF for $Re = 3.0$, $a = 1.28$, $m = 0.00166$, $\zeta = 1.1$, $J = 0.0795$, $K = -0.9993$, wavenumber $\alpha = 2$. (*b*) The calculated hold-up ratio h against time. At $t = 0$, the PCAF hold-up ratio $h = 2.61$. As PCAF evolves, h decreases first and stabilizes around 1.46.

be manually controlled and made to stay constant. We believe that the simulation started from PCAF can match the experiments if we know the experimental quantities $[a, f]$. Unfortunately, the driving pressure gradient for figure 6 of Bai *et al.* (1996) is not available, and we are not able to determine the PCAF by prescribing $[a, f]$. Rather, we solve an inverse problem here with a variety of larger Reynolds numbers to find the experimental result.

The solution of the inverse problem is discussed next. Figure 9(*a*) shows the base velocity field for PCAF at $Re = 3.0$, $K = -0.9993$. This is fully up-flow, in both fluids. The PCAF hold-up ratio h is 2.61. We performed a calculation for this flow from an initial amplitude $A(0) = 0.005$ on a 256×256 mesh. The wavenumber is 2. The evolution of the hold-up ratio with the time is shown in figure 9(*b*). The hold-up ratio decreases dramatically between $t = 20$ and $t = 40$. This period corresponds to the transition from the linear regime to the nonlinear regime, as we reported before. In the fully nonlinear bamboo wave regime, the hold-up ratio stabilizes around 1.46, which is a reasonable approximation of the experimental value 1.39. A final remark on the hold-up ratio: two additional cases were run, with $K = -1.2$ and $K = -1.4455$ (Reynolds number $Re = 3.5$ and $Re = 4.0$, respectively), and hold-up ratios of 1.46 and 1.45, respectively, were obtained.

Theoretical treatments such as the linear and weakly nonlinear theories apply only for limiting situations, while experimental results do not reveal all the details of the solution, and therefore it is the role of numerical simulations to fill this gap and to provide insight into core–annular flows in the nonlinear regime. The interface position at $t = 100$ is plotted in figure 10(*a*), and is very similar to the one in figure 7 for $\alpha = 2.0$, $Re = 0.93$, with the crest a little more pointed. To investigate the flow field in more detail, we examine the streamlines and contours of the pressure field. For an incompressible fluid, the axisymmetric stream function ψ is defined by the following formulas:

$$u = -\frac{1}{r}\frac{\partial \psi}{\partial x}, \quad v = \frac{1}{r}\frac{\partial \psi}{\partial r}.$$

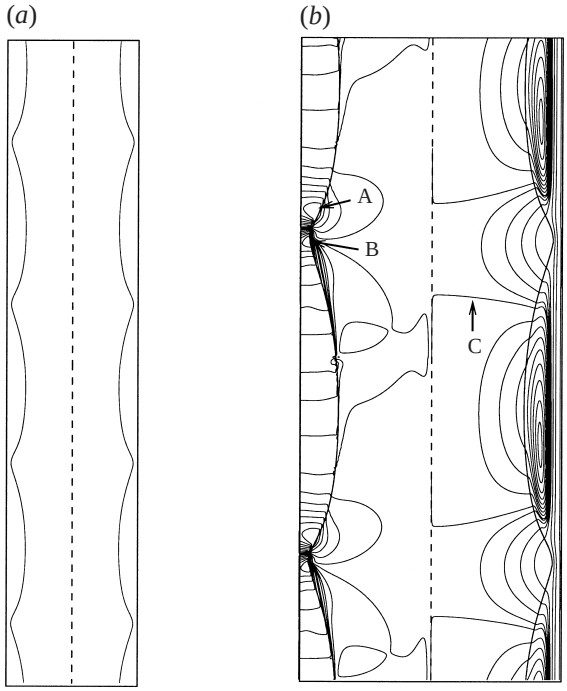

FIGURE 10. Up-flow for $Re = 3.0$, $a = 1.28$, $m = 0.00166$, $\zeta = 1.1$, $J = 0.0795$ and $K = -0.9993$. (*a*) Interface shape at $t = 100$. (*b*) Pressure contours on the left half. Pressure field reaches the maximum value on the upper side of the crest, at location A and the minimum value on the down-side of the crest, at location B. Streamlines in the frame of reference moving with the oil core are shown on the right half. The broken line represents the axis of symmetry.

This function is calculated numerically by a standard central difference scheme. In the left half of figure 10(*b*), we plot the contours of the pressure field. In the water, the pressure field reaches its maximum value above the crest, at location A and its minimum value below the crest, at B. This confirms the schematic explanation in figure 15.5 in Joseph & Renardy (1993). From below the crest to above, the pressure increases monotonically in the water. Thus, the pressure contours are nearly horizontal lines. The pressure field in the oil core is also shown in the figure. In the right half of figure 10(*b*), we plot the streamlines in the frame of reference moving with the oil core. The average velocity of the oil core is 0.685 at this time. C denotes a line which divides the set of streamlines into two categories. One category is inside the line and forms a recirculation zone; the other is outside. While some of them are completely in the water, others enter into the oil on the upper side of the crest and return to the water on the lower side of crest. The behaviour of these streamlines is due to the fact that the waves move slowly compared to the oil core. The wave speed c is 0.614, which is 10% smaller than the core velocity. The flow is not stationary.

In the preceding Sections, our numerical method was validated against theory, and simulation results were compared with experimental results. In the following, we delve further into the physics of core–annular flow in the bamboo wave regime.

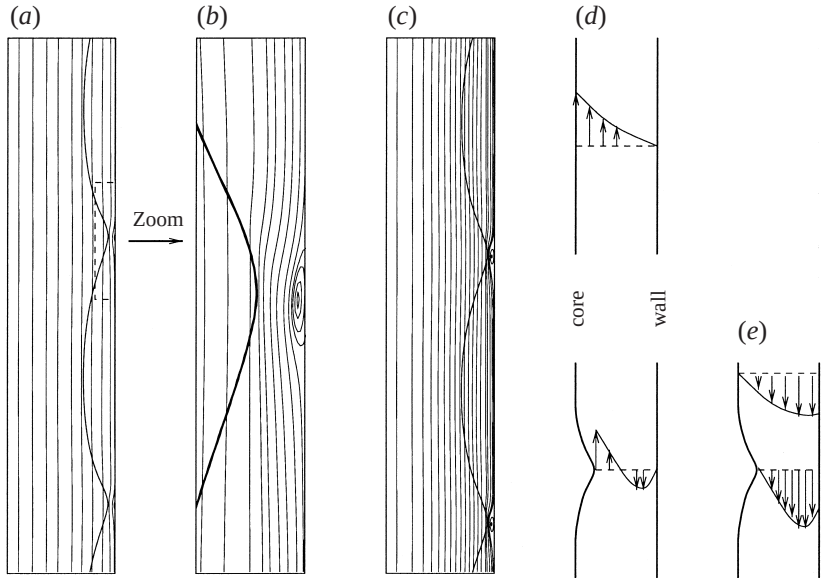

FIGURE 11. Streamlines are drawn in the frame of reference fixed with the wall. Vortices appear near the crests. (*a*) $Re = 3.0$ flow for one axial wavelength. (*b*) Zoom of dashed zone. (*c*) $Re = 1.7$ flow, showing more pronounced vortices. (*d*) Schematic of velocity profiles in the water in the frame of reference fixed with the wall. Upper plot shows the PCAF regime, and the lower plot shows mixed flow for the bamboo wave regime. (*e*) Schematic in the frame of reference fixed with the core.

6.1. *Vortex near the wall*

We have seen in the previous Section that the pressure field reaches its maximum value just above the crest and its minimum value just below (figure 10). These extreme points are near the oil core but in the water. Therefore, the pressure pushes the water toward the wall at the upper side of the crest and pulls it from the wall at the lower side. This feature in the water creates a interesting pattern of flow if the wave crests are near the pipe wall. At $Re = 3.0$, we find small vortices near the wave crests in the frame of reference fixed with the wall (figure 11*a, b*). These vortices are more prominent for smaller Reynolds number flows. For example, figure 11(*c*) shows the case $Re = 1.7$, where the vortices are larger than at $Re = 3$ and located centrally at the crests, while the vortices at $Re = 3.0$ are compressed against the pipe wall. The schematic in figure 11(*d*) explains the origin of these vortices. The PCAF is an up-flow. Since $f + \rho_2 g < 0$, the drag from the oil core plays an important role, and the driving pressure gradient alone is not enough to sustain the up-flow in the water. As the flow evolves into the nonlinear regime, the oil core is slowed down and therefore it drags less water. The slowing down of the core is so significant that a mixed flow is produced, in which the water falls down near the pipe wall and rises near the core.

This argument accounts for the mixed flow, but does not explain why the vortices appear at the crests and not at the troughs. To explain that aspect, we examine the flow in the frame of reference where the core is fixed. In such a reference frame, the core forms a stationary boundary, while the wall is moving downward at constant speed. Consequently, a shear flow develops in the water, driven by a combination of the downward wall speed and the downward action of gravity. The profile is sketched schematically in figure 11(*e*). We note that mass conservation requires a

larger downward speed at the crests, where the cross-section is narrow, than at the troughs, where the cross-section is wide. Thus, if downward speeds larger than the wall speed occur, they will first occur at the crests. When the frame of reference is switched back to the laboratory frame (figure 11*d*), there is a mixed profile at the crests, leading to the appearance of vortices.

6.2. *Effect of a and temporally periodic flow*

In the investigations of the previous Sections, the radius ratio is $a = 1.28$ so that the oil core is relatively close to the pipe wall and the interaction between them is strong, leading to the vortices found near the wave crests. In this Section, we address what happens if the oil core is relatively far away from the pipe wall, so that the water has a large 'living room'. For this purpose, consider the experimental data point no. 1 in figure 3, where $a = 1.61$, $F = -1.0577$, which correspond to $J = 0.063354$, and $K = -2.0303$. The centreline velocity for PCAF is $V_0^*(0) = 83.91$ cm s^{-1} so our Reynolds number is $Re_1 = 3.73754$. Linear theory indicates that the most dangerous mode for this flow has wavenumber $\alpha = 2.4$, corresponding to a wavelength $L = 2.618$. The growth rate $\mathrm{Re}(\sigma) = 0.066$ is much less than the $a = 1.28$ case, where the oil core is closer to the pipe wall. We set the initial amplitude of perturbation $A(0) = 0.01$. The evolution of the maximum amplitude $A(t)$ with the time is plotted, on a $\log_{10}$-linear scale, in figure 12(*a*). The calculation is carried out on a 256×256 mesh over one spatial period on a domain $[0, 1.61] \times [0, 2.618]$. The initial growth of the perturbation compares well with the predicted linear theory, and then begins to deviate as the amplitude increases. After roughly 40 s, a fully nonlinear evolution begins to take shape. Since the initial amplitude is chosen relatively large, we do not expect the type of exact replication of linear growth rates that we saw in figure 5. Linear theory yields a wave speed 0.9542, and the numerical wave speed is 0.9431 initially, and 0.8068 at time $t = 200$ (figure 12*b*).

The corresponding interface profiles are shown in figure 13 at $t = 0$, 20, 30, 60 and 120. At $t = 20$, the interface is still in the linear regime and has a sinusoidal shape. The interface shape at $t = 30$ reveals some asymmetry, in that the interface crest is narrower than the trough. This can be explained by the fact that the low-viscosity water provides less resistance, making it easier for the high-viscosity oil to penetrate into it. An analogy is that when inertia is important, a high-density fluid penetrates easily into a low density-fluid. Soon after the flow enters the nonlinear regime, the interface appears to reach its maximum amplitude and the shape reaches equilibrium. The interfaces at time $t = 60$ and $t = 120$ are similar.

The most surprising feature of this flow is that it demonstrates temporal periodicity, as evident from the evolution of the hold-up ratio vs. time (figure 12*c*). As the PCAF evolves into the nonlinear bamboo wave regime, the hold-up ratio first decreases. After a relatively long transition period, the hold-up ratio begins to oscillate around 2.15, with a well-defined temporal period of about 8.

The temporal periodicity of the flow is investigated in detail by viewing the streamlines. Figure 14 shows the streamlines from $t = 188$ to $t = 197$. They constitute one complete period and are drawn in the frame of reference moving with the core. The flow regime is unsteady and we distinguish two qualitatively different streamline patterns, with one large vortex or two small vortices in each trough. Let us begin the flow pattern study from $t = 188$. We see one large vortex. Unlike the vortices observed in the previous Section, this vortex will not rest at the same place but be convected downstream by the flow ($t = 189$ and $t = 190$). The vortex is compressed by the flow against the upper side of the crest and can no longer move downstream. Meanwhile,

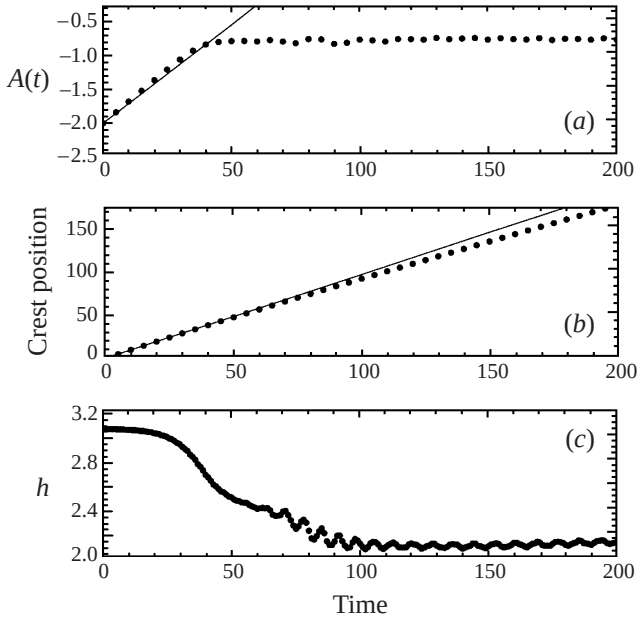

FIGURE 12. Up-flow for $\alpha = 2.4$, $Re_1 = 3.73754$, $a = 1.61$, $m = 0.00166$, $\zeta = 1.1$, $J = 0.063354$, and $K = -2.030303$. For the interfacial mode, theoretical linear growth rate is 0.066 and wave speed 0.954. (*a*) Maximum amplitude $A(t)$ vs. time on a $\log_{10}$-linear scale. (*b*) Wave crest position vs. time. (*c*) Hold-up ratio vs. time. The hold-up ratio oscillates around 2.15, with period approximately 8. Solid line represents theoretical growth and circles represent the calculation carried out on a 256×256 mesh.

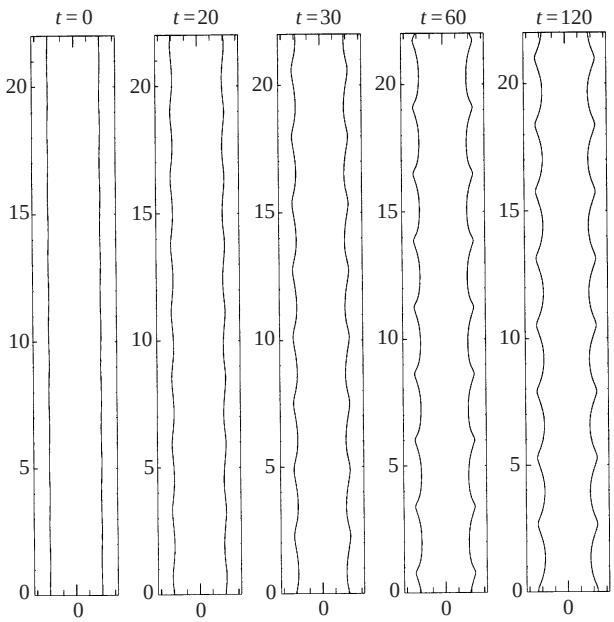

FIGURE 13. Sequence of interface positions for $Re_1 = 3.73754$, $a = 1.61$, $m = 0.00166$, $\zeta = 1.1$, $J = 0.063354$ and $K = -2.030303$: $t = 0$, 20, 30, 60 and 120. The calculation is carried out on a 256×256 mesh.

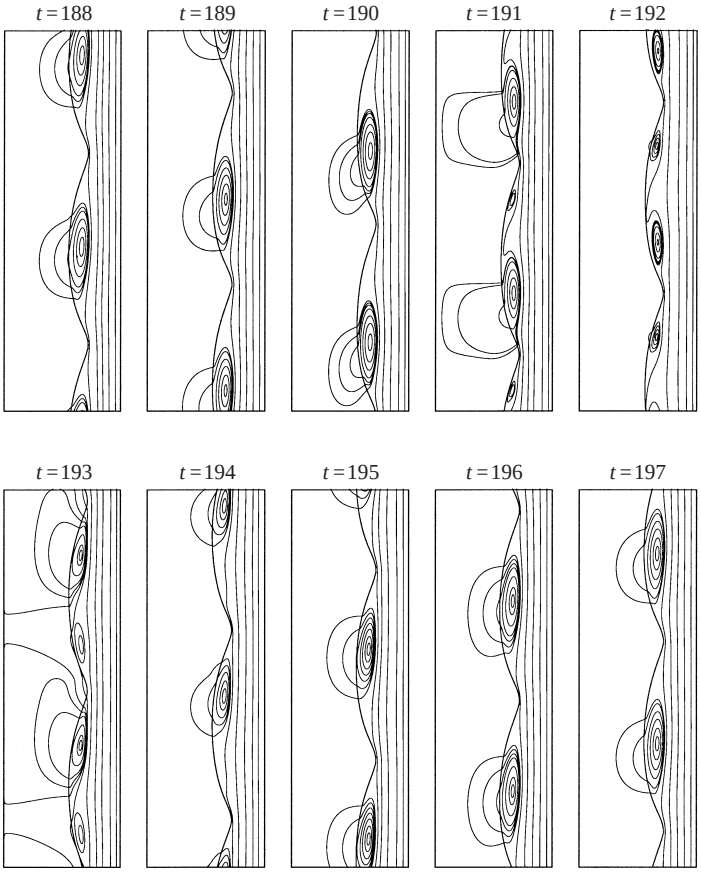

FIGURE 14. Up-flow for $Re = 3.74$, $a = 1.61$, $m = 0.00166$, $\zeta = 1.1$, $J = 0.063354$ and $K = -2.030303$. Unsteady regime, showing one complete temporal period. The period is about 8.

a small vortex is created on the other side of the crest ($t = 191$). While the upper-side vortex continues to reduce its size, the lower-side vortex gains ground ($t = 192$ and $t = 193$). At $t = 194$, the upper-side vortex has completely disappeared. The picture at $t = 196$ shows one large vortex settling in the middle of the trough and completes one whole period. We should remark that the one-vortex pattern corresponds to the valley of the hold-up ratio chain (figure 12*c*) and the two-vortices pattern corresponds to the summit. In the one-vortex pattern, the flow is well organized and so the water flow rate increases (hold-up ratio decreases), while in the two-vortices pattern, the flow is in disorder, and so the water flow rate decreases (hold-up ratio increases).

6.3. *Effect of Re and temporally periodic flow*

We continue the study of flow features, varying the Reynolds number and keeping the others parameters constant. The calculations are performed for the most unstable modes. The Reynolds numbers and the corresponding wavenumbers are listed in table 2. The wavenumber for the fastest growing mode decreases as the Reynolds number increases. The corresponding nonlinear wave shapes are shown in figure 15. We find that the slow and long waves (low Reynolds number flow) have asymmetrical crest shape, flat on the upper side and steeper on the lower side. This asymmetry

Re	1.0	1.5	2.0	3.0	3.74
α	0.9	1.18	1.45	1.95	2.4

TABLE 2. The Reynolds numbers and the corresponding wavenumbers for the most unstable modes according to linear theory, $a = 1.61$, $m = 0.00166$, $\zeta = 1.1$, $J = 0.063354$ and $K = -2.030303$.

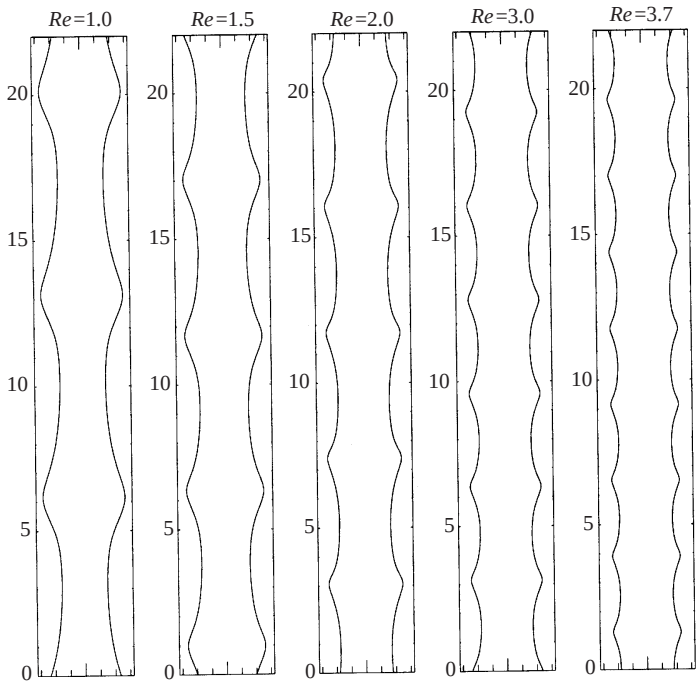

FIGURE 15. Up-flow for $a = 1.61$, $m = 0.00166$, $\zeta = 1.1$, $J = 0.063354$ and $K = -2.030303$.

is due to the effect of the buoyancy. In fast flow (large Reynolds number flow), the asymmetric effect of buoyancy is relatively less important, as evident in the almost symmetric shape of wave crests for $Re = 3.74$.

Figures 16 and 17 illustrate the interface position, together with streamlines on the right half and pressure contours on the left half, only in the water. We observe no vortex in the frame of reference fixed with the pipe wall. The streamlines here are drawn in the frame of reference moving with the oil core. Low Reynolds number flows ($Re = 1.0$ and $Re = 1.5$) are similar to the case $a = 1.28$, with one large vortex settling in each wave trough. The pressure contours are almost horizontal, with maximum (minimum) value on the upper (lower) side of the crest. While the $Re = 2.0$ flow keeps almost all these features, we observe a change in the pressure pattern, with the appearance of some pressure summits and valleys. At $Re = 3.0$, figure 17 shows the same type of temporally periodic streamline pattern as $Re = 3.74$ in figure 14. The temporal period is about 10. A pressure valley occurs in the large vortex, near its centre ($t = 152$), while a pressure summit appears between the two small vortices and seems to assume the role of keeping them apart ($t = 158$). The evolution of hold-up

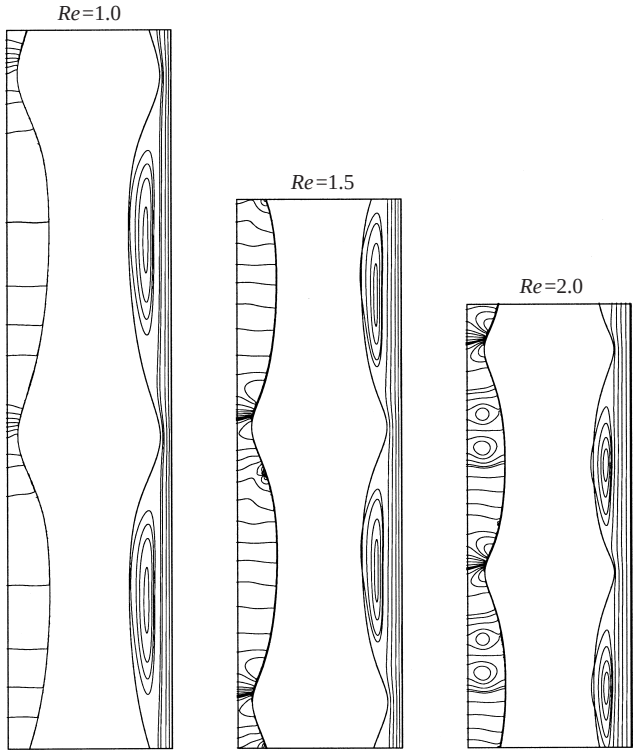

FIGURE 16. Up-flow for $Re = 1.0$, 1.5 and 2.0, $a = 1.61$, $m = 0.00166$, $\zeta = 1.1$, $J = 0.063354$ and $K = -2.030303$. Steady regime.

ratio of these flows is shown in figure 18. While the periodicity has started to appear in low Reynolds number flow ($Re = 1.0$, 1.5 and 2.0), it becomes quite marked in the $Re = 3.0$ flow.

7. Down-flow

In down-flow, the pressure and buoyancy forces of oil oppose those of water. This tends to compress, even eliminate, bamboo waves. The stems thicken into columns of oil which are perturbed by corkscrew waves from place to place. This flow type is called 'disturbed core–annular flow'. It was first reported in the experiment of Bai *et al.* (1992). The down-flow with parameters $Re = 1.2$, $a = 1.7$, $m = 0.00166$, $\zeta = 1.1$, $J = 0.06$ and $K = -0.542709$ was investigated by Renardy (1997) in the context of non-axisymmetric perturbations, which was earlier studied by Hu & Patankar (1995). They showed that mode 1 has the largest growth rate at $\alpha = 0.531$ and mode 0 has much smaller growth rates, though it has two bands of unstable wavelengths, one for long waves due to interfacial tension and the other at $O(1)$ wavenumbers due to shear. They showed that the wavelengths and wave speeds agree with the experimental values. We investigate this flow under the axisymmetric assumption. Linear theory indicates that the most dangerous axisymmetric mode has wavenumber 1.4, and we treat core–annular flow seeded with this eigenmode. We cover a range of Reynolds numbers while keeping the relative driving forces K constant. We expect that the

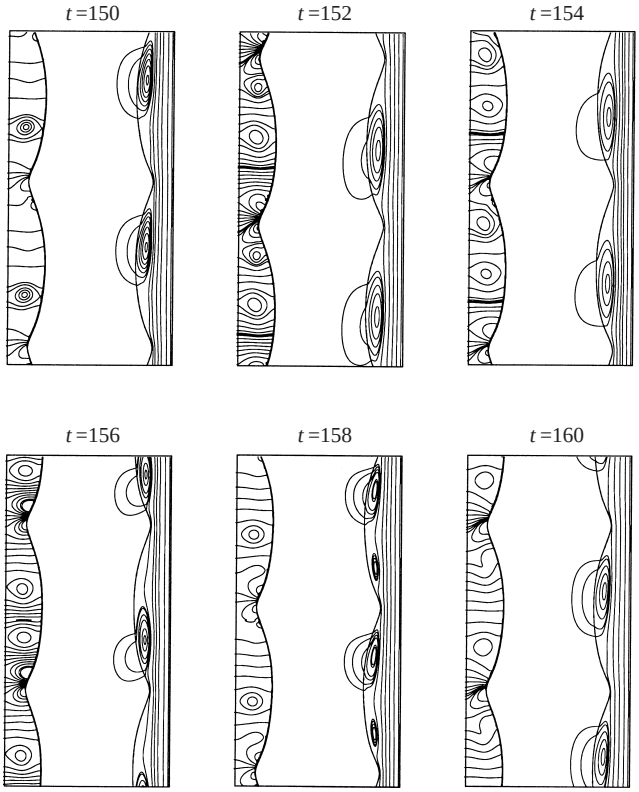

FIGURE 17. Up-flow for $Re = 3.0$, $a = 1.61$, $m = 0.00166$, $\zeta = 1.1$, $J = 0.063354$ and $K = -2.030303$. Unsteady regime, showing one complete period. The period is about 10.

Re	1.2	2.0	2.5	3.0
α	1.4	1.675	1.975	2.625
$\mathrm{Re}(\sigma)$	0.0207	0.0355	0.0415	0.0455
Amplitude	0.133	0.1412	0.166	0.155

TABLE 3. Reynolds numbers and corresponding axisymmetric wavenumbers of largest growth rates, for $a = 1.7$, $m = 0.00166$, $\zeta = 1.1$, $J = 0.06$ and $K = -0.542709$.

asymmetric effect of buoyancy on the core–annular flow is less important in fast flow (high Reynolds number). The Reynolds numbers and the corresponding wavenumbers of the most unstable mode and the growth rates according to linear theory are listed in the table 3. The wavenumber increases, and hence the wavelength decreases, with the Reynolds number. Growth rates increase with the Reynolds number.

The base velocity profile for PCAF (see equation (3.3)) does not depend on the parameters *Re* and *J*, and all the flows in table 3 share the same profile shown in figure 19. This is a mixed flow in the frame of reference moving with the oil core, because the water is heavier than the oil and so falls faster than the oil near the core. On the other hand, the water velocity must match the boundary condition near the pipe wall and therefore it moves slowly near the wall. This down-flow configuration of

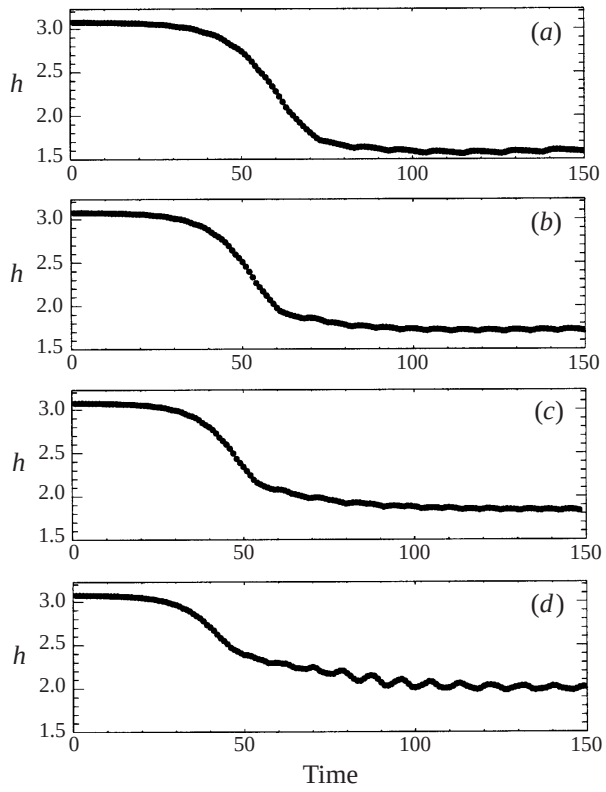

FIGURE 18. Hold-up ratio for up-flow $a=1.61$, $m=0.00166$, $\zeta=1.1$, $J=0.063354$ and $K=-2.030303$. The Reynolds number are (*a*) $Re=1.0$, (*b*) $Re=1.5$, (*c*) $Re=2.0$ and (*d*) $Re=3.0$.

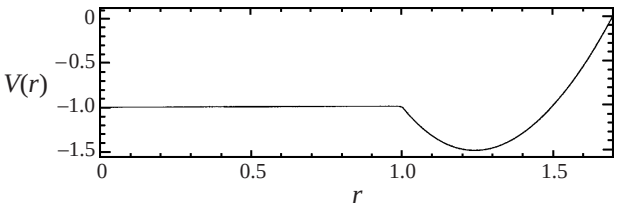

FIGURE 19. PCAF velocity profile for down-flow for $a = 1.7$, $m = 0.00166$, $\zeta = 1.1$, and $K = -0.542709$. The PCAF base velocity does not depend on Re and J.

PCAF would introduce some significant consequences for the corresponding nonlinear waves. Numerical investigation of these flows is performed on a 256×256 mesh. We set the initial amplitude $A(0) = 0.01$. These waves attain an equilibrium shape soon after they evolve into the nonlinear regime, as shown in figure 20. For slow flow, $Re = 1.2$, the saturation amplitude is small, and the interface is merely perturbed from the PCAF form. However, the asymmetry of the crest is prominent, due to the effect of buoyancy of oil relative to water, which flattens the up-side (back) of the crest and steepens the down-side (front) of the crest. When the Reynolds number increases, inertia gains importance and reduces the asymmetric effect due to the buoyancy, the wave amplitude increases and the wave shape becomes more symmetric. Differences in wave shape between up- and down-flow vanish for $Re = 3$.

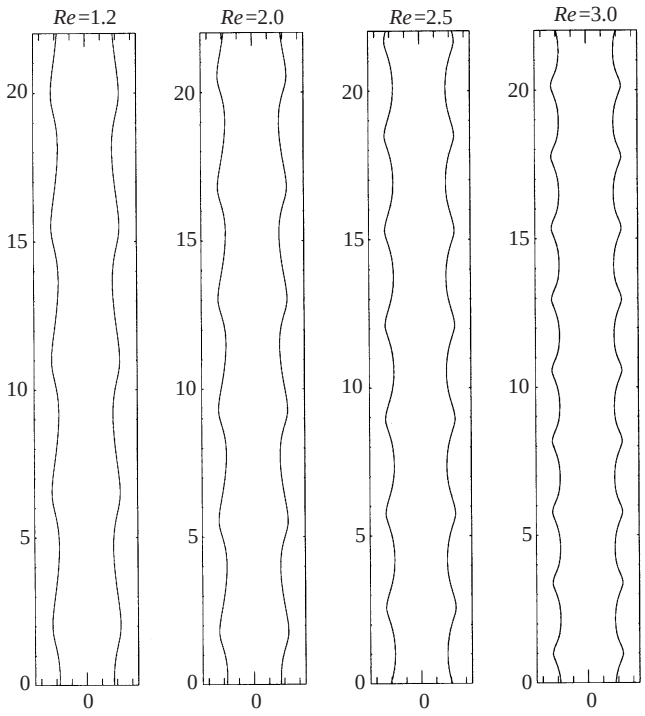

FIGURE 20. Down-flow for $a = 1.7$, $m = 0.00166$, $\zeta = 1.1$, $J = 0.06$ and $K = -0.542709$.

When the driving pressure gradients are relatively large and the flow is fast, Bai *et al.* (1992) mention that the difference between up- and down-flow vanishes. Here, we have kept the driving pressure forces constant (K constant), so that the flow is faster when the viscosity reduces (Reynolds number rises). We find that the down-flow pattern is qualitatively different from the up-flow one, even for fast down-flow where wave shapes look like the up-flow ones. In figure 21, we plot the contours of the pressure field in the left half and the streamlines in the right half. For $Re = 1.2$, we observe a vortex on the front side (lower side) of crests in the frame of reference moving with the oil core. This vortex is located in a strong shear layer and its formation is due to the mixed flow profile that we described before. Accordingly, the pressure reaches the minimum value at the centre of this vortex. The pressure maximum value is on the back of the wave crest. Compared to the up-flow wave, the extremal values of the pressure have switched their locations. These features are retained for the higher Reynolds numbers we have examined, in contrast to the up-flow case where the flow patterns for $Re = 3.0$ and 3.74 are different. In summary, slow down-flow leads to low-amplitude asymmetric waves. Fast down-flow leads to bamboo waves but with the pressure field qualitatively different from the up-flow bamboo waves.

8. Conclusion

Our numerical simulation of bamboo waves represents an improvement on the simulations of Bai *et al.* (1996), who solved for the steady solution of the governing equations, assuming density matching, and a solid core. We have relaxed those

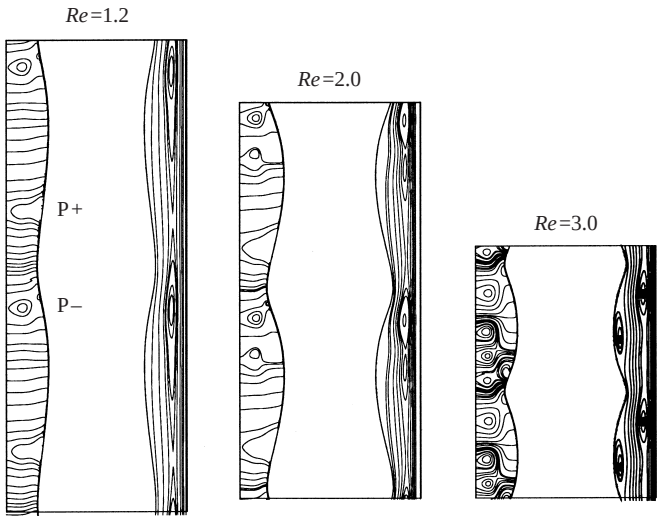

FIGURE 21. Down-flow for $a = 1.7$, $m = 0.00166$, $\zeta = 1.1$, $J = 0.06$ and $K = -0.542709$. Pressure contours on the left half and streamlines in the frame of reference moving with oil core on the right half.

assumptions, allowing for different densities for the two viscous liquids, and we use the experimental parameters for the simulation of nonlinear regimes. We assume axisymmetry. Our initial condition is seeded with an eigenmode of largest growth rate, and results for other modes are also shown to lead to bamboo waves. The bamboo waves arise at the fully nonlinear saturation of the initial value problem. We have in addition reproduced the unique bamboo structure of the waves with pointed peaks. The question of how to choose the model parameters is investigated and has revealed an alternative approach where an inverse problem is solved and predicts a satisfactory value for the experimental hold-up ratio.

This research was sponsored by the National Science Foundation under Grant CTS-9612308. We thank C. Appert of l'École Normale Supérieure for discussion on the adaptation of our semi-implicit scheme to the axisymmetric case, and Michael Renardy for general discussions.

REFERENCES

BAI, R., CHEN, K. & JOSEPH, D. D. 1992 Lubricated pipelining: stability of core–annular flow. part 5. experiments and comparison with theory. *J. Fluid Mech.* **240**, 97–142.

BAI, R., KELKAR, K. & JOSEPH, D. D. 1996 Direct simulation of interfacial waves in a high-viscosity-ratio and axisymmetric core–annular flow. *J. Fluid Mech.* **327**, 1–34.

BRACKBILL, J. U., KOTHE, D. B. & ZEMACH, C. 1992 A continuum method for modeling surface tension. *J. Comput. Phys.* **100**, 335–354.

COWARD, A. V., RENARDY, Y., RENARDY, M. & RICHARDS, J. R. 1997 Temporal evolution of periodic disturbances in two-layer couette flow. *J. Comput. Phys.* **132**, 346–361.

GUEYFFIER, D., LI, J., NADIM, A., SCARDOVELLI, R. & ZALESKI, S. 1999 Volume of fluid interface tracking and smoothed surface stress methods applied to multiphase flow and pendant drop pinching. *J. Comput. Phys.* to appear.

HU, H. & PATANKAR, N. 1995 Non-axisymmetric instability of core–annular flow. *J. Fluid Mech.* **290**, 213–234.

JOSEPH, D. D., BAI, R., CHEN, K. & RENARDY, Y. Y. 1997 Core–annular flows. *Ann. Rev. Fluid Mech.* **29**, 65–90.

Joseph, D. & Renardy, Y. 1993 *Fundamentals of Two-Fluid Dynamics, Part II*. Springer.

Lafaurie, B., Nardone, C., Scardovelli, R., Zaleski, S. & Zanetti, G. 1994 Modelling merging and fragmentation in multiphase flows with surfer. *J. Comput. Phys.* **113**, 134–147.

Li, J. 1995 Calcul d'interface affine par morceaux (piecewise linear interface calculation). *C. R. Acad. Sci. Paris* **320** (IIb), 391–396.

Li, J., Renardy, Y. & Renardy, M. 1998 A numerical study of periodic disturbances on two-layer couette flow. *Phys. Fluids* **10**, 3056–3071.

Peyret, R. & Taylor, T. D. 1990 *Computational Methods for Fluid Flow*. Springer.

Renardy, M. 1992 A possible exlanation of bamboo waves in core–annular flow of two liquids. *Theor. Comput. Fluid Dyn.* **4**, 95–99.

Renardy, Y. 1997 Snakes and corkscrews in core–annular down-flow of two fluids. *J. Fluid Mech.* **340**, 297–317.